ACS APPLIED MATERIALS & INTERFACES

www.acsami.org Research Article

Understanding the Structure−Performance Relationship of Lithium-Rich Cathode Materials from an Oxygen-Vacancy Perspective

Shao-Lun Cui, Xu Zhang, Xue-Wen Wu, Sheng Liu, Zhen Zhou, Guo-Ran Li,* and Xue-Ping Gao

Cite This: https://dx.doi.org/10.1021/acsami.0c14979 Read Online

ACCESS | Metrics & More | Article Recommendations | Supporting Information

ABSTRACT: Li-rich layered oxide cathode materials are regarded as an attractive candidate of next-generation Li-ion batteries (LIBs) to realize an energy density of >300 Wh kg^{-1}. However, challenges such as capacity fade, cycle life, oxygen release, and structural transformation still restrain its practical application. Micro/nanotechnology is one of the effective strategies to enhance its structural stability and electrochemical performance. An in-depth understanding of the relationship between micro/nanostructures and the electrochemical performance of Li-rich layered oxides is undoubtedly important for developing high-performance cathode materials. Herein, $Li_{1.2}Ni_{0.13}Co_{0.13}Mn_{0.54}O_2$ with different micro/nanostructures including irregular particles, microspheres, microrods, and orthogonal particles are synthesized. Starting from the amount of surface oxygen vacancies in the different structures, the influence of oxygen vacancies on every step during the charge−discharge processes is analyzed by experimental characterizations and theoretical calculations. It is indicated that intrinsic oxygen vacancies can enhance the electrical conductivity and decrease the energy barrier for ion migration, which exerts a significant influence on promoting the kinetics and capacity. Among the different micro/nanostructures, microrods with abundant oxygen vacancies can not only promote lithium ion transport but also stabilize a cathode electrolyte interface (CEI) film by adjusting the distribution of surface elements with lower nickel content. The microrods deliver an initial discharge capacity of up to 306.1 mAh g^{-1} at 0.1C rate and a superior cycle performance with a capacity retention of 91.0% after 200 cycles at 0.2C rate.

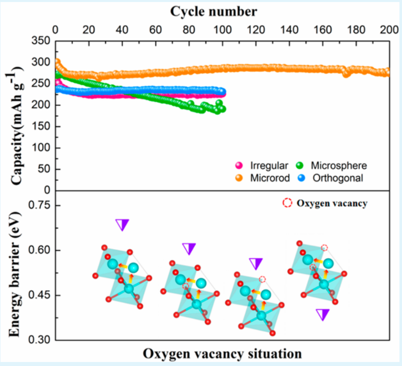

KEYWORDS: *morphology, structure−performance relationship, oxygen vacancy, Li-rich cathode material, Li-ion battery, micro/nanotechnology*

1. INTRODUCTION

Li-ion batteries (LIBs) have become a dominant power source for electric vehicles and portable electronic products. However, the developing electric vehicles are badly in need of new rechargeable batteries with a high energy density of >300 Wh kg^{-1}, which is not available for current commercial lithium-ion batteries.[1−3] To meet the requirement of battery energy density, new cathode materials with significantly increased capacity are necessary. Compared with the traditional layered $LiCoO_2$, spinel $LiMn_2O_4$, and olivine $LiFePO_4$ cathode materials with specific capacities of <200 mAh g^{-1}, Li-rich layered oxides ($xLi_2MnO_3\cdot(1-x)LiMO_2$, M = Ni, Co, Mn, etc.) are emerging as one of the most competitive candidates to satisfy the energy requirements owing to their distinguished specific capacity exceeding 250 mAh g^{-1}.[4−7] Nevertheless, they still suffer from low initial Coulombic efficiency, sluggish reaction kinetics, poor cycle life, and severe structural degradation.[8,9] Also, phase transformation from the layered structure to the spinel or even rock-salt phases greatly influences the internal structural stability and leads to active material failure.[10] To solve these problems, efforts such as micro/nanostructure design, surface coating, and bulk doping have been made in recent years. Among these methods, micro/nanostructure design is considered one of the most promising approaches to improving the intrinsic stability and enhancing the electrochemical performance of Li-rich materials with reduced cost.[11,12] Nanoscale primary particles can not only increase contact area and ensure sufficient penetration at the interface of cathode materials and electrolyte but also shorten the lithium ion diffusion path, thereby accelerating charge transfer.[13−15] Simultaneously, the regular arrangement of microscale secondary particles is effective in improving the structural stability of the electrode materials and the texture properties for ion transfer in electrodes. However, the small size and exposure of certain crystal planes for micro/nanostructures can have an adverse effect on cycling stability. The structure−performance relationship is important but complicated, and an in-depth understanding is still necessary for developing high-performance Li-rich cathode materials.

Received: August 19, 2020
Accepted: September 28, 2020

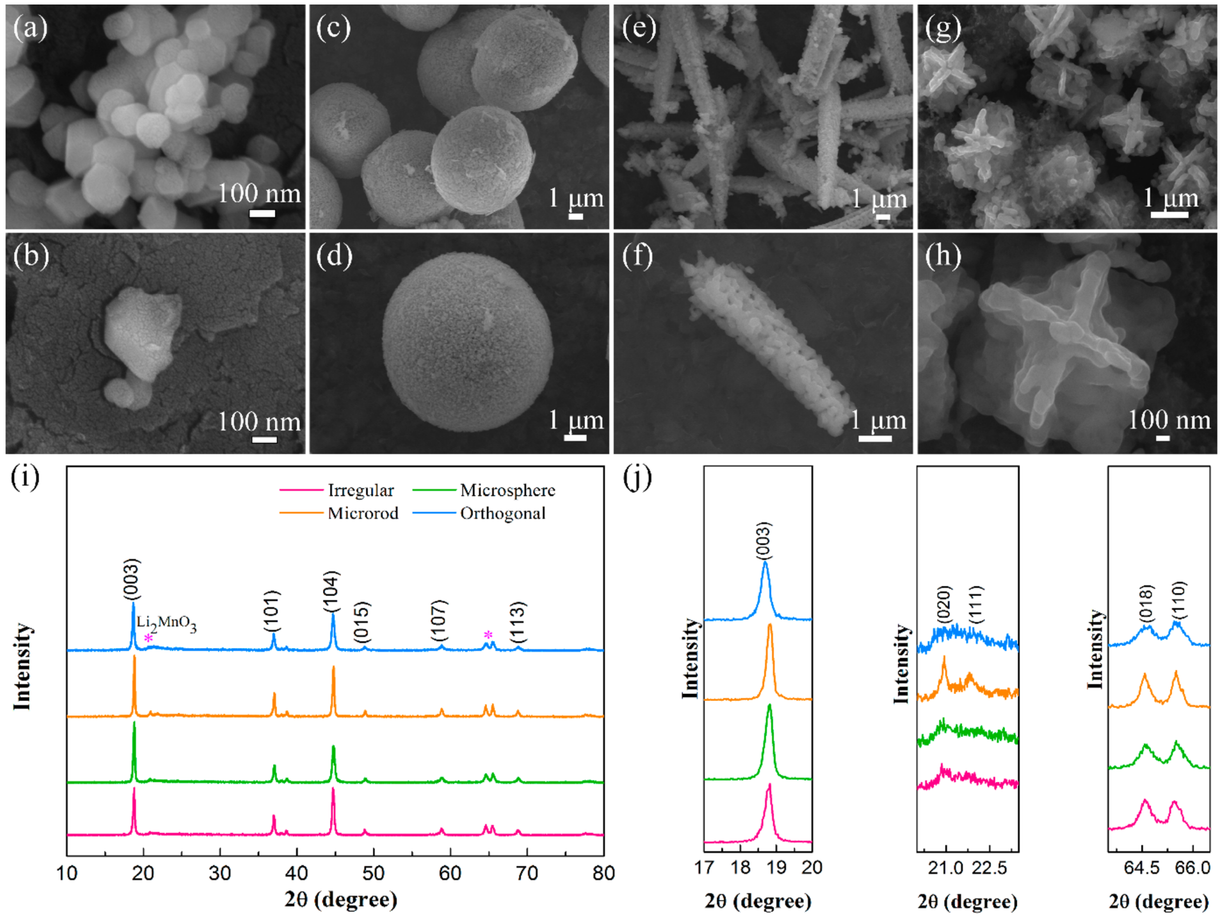

Figure 1. SEM images (a−h) and XRD patterns (i, j) of irregular, microsphere, microrod, and orthogonal Li-rich cathode materials.

Mn-based Li-rich cathode materials exhibit a unique dual-redox mechanism of both cations and anions. During the first charge process, the Li_2MnO_3 component is activated and represents an obvious voltage plateau at 4.5 V accompanied by irreversible oxygen release and structural changes.[13,16,17] Previous studies have revealed that intrinsic oxygen vacancies are verified to suppress irreversible oxygen loss over cycling, which contributes to higher initial Coulombic efficiency.[13,18] Furthermore, intrinsic oxygen vacancies formed on the surface give rise to an imbalanced charge distribution, thus facilitating the insertion/extraction of lithium ions and enhancing the electrical conductivity of cathode materials.[13] Besides, after finishing the first discharge stage, part of the Mn^{4+} species will be reduced to Mn^{3+} as charge compensation, which triggers the Jahn−Teller effect and results in distortion of the molecular configuration with the increase of internal stress and the appearance of harmful cracks.[19,20] Another study reveals that higher nickel content on the surface is prone to induce the interaction between Ni^{4+} and the electrolyte, especially under the highly charged state, which leads to complicated interfacial side reactions at the same time.[3] Meanwhile, intrinsic oxygen vacancies on the surface of the cathode materials can provide a favorable ion diffusion and electron transport environment and hinder the layered-to-spinel phase transition, thus supporting higher capacity and energy output.[13,21−26] Therefore, it is interesting and worthwhile to discuss the relationship between micro/nanostructures and electrochemical performance from oxygen-vacancy perspective.

In this work, $Li_{1.2}Ni_{0.13}Co_{0.13}Mn_{0.54}O_2$ cathode materials with four different micro/nanostructures are synthesized, characterized, and investigated as cathode materials for lithium ion batteries. With close surface area, the samples have various contents of intrinsic oxygen vacancies on the surfaces with different micro/nanostructures. It is found that intrinsic oxygen vacancies on the surface are beneficial to reduce the ion migration energy barrier and accelerate the kinetics process. Moreover, an intrinsic oxygen vacancy generates processive influence during the charge−discharge process of the cathode material. The microrods with abundant oxygen vacancies can effectively suppress the Jahn−Teller distortion effect, thereby effectively improving the structural stability. In addition, phase transformation from layered to spinel structures is also markedly alleviated in the cycled microrods with a thin cathode electrolyte interface film. The effects of oxygen vacancy in the whole electrochemical process promote the prepared microrods to exhibit a discharge capacity of up to 306.1 mAh g^{-1} at 0.1C rate (1C = 200 mA g^{-1}) and a superior cycling performance with a capacity retention of 91.0% (274 mAh g^{-1}) after 200 cycles at 0.2C rate. The results provide a new perspective to understand the structure−performance relationship of lithium-rich cathode materials and are helpful for the development of high-performance energy storage materials for lithium-ion batteries.

2. RESULTS AND DISCUSSION

The detailed synthesis route and methods of four different morphological samples are illustrated in the Supporting

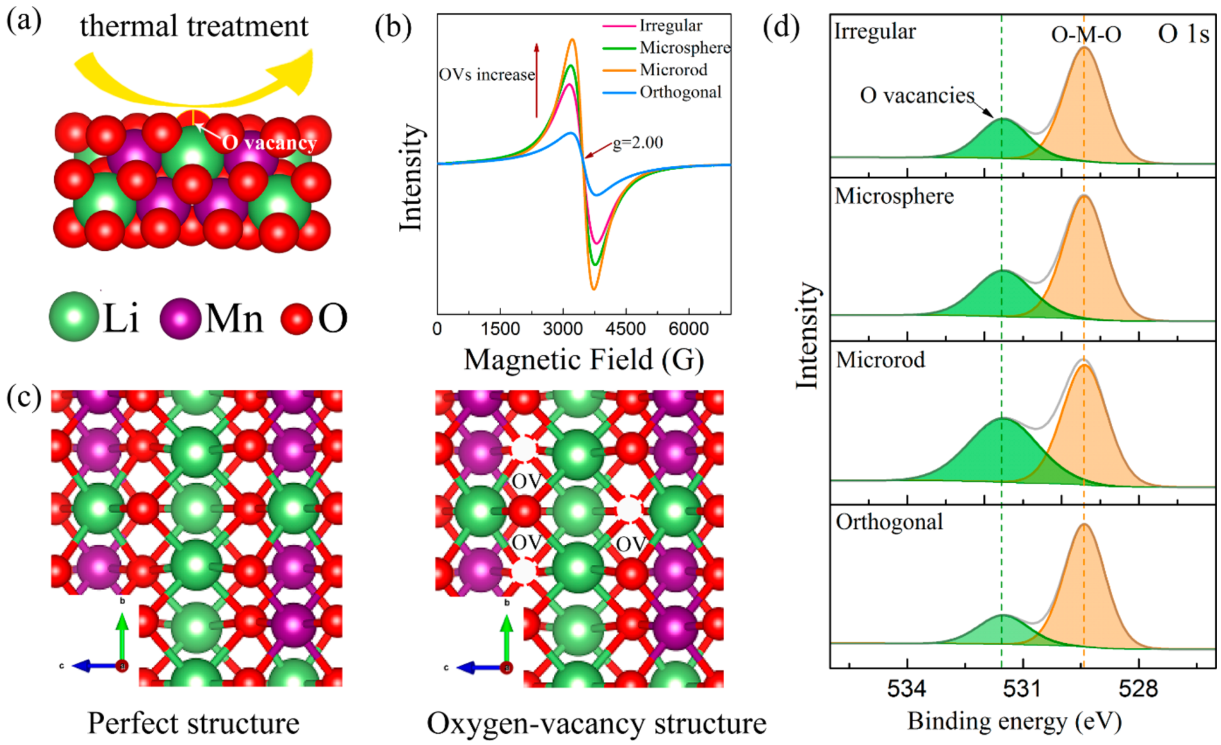

Figure 2. (a) Schematic of oxygen-vacancy formation. (b) EPR spectra of different morphological particles. (c) Illustration of perfect structure and oxygen-vacancy structure based on the Li_2MnO_3 model. (d) XPS spectra of O 1s of different morphological particles.

Information. Irregular particles, microspheres, microrods, and orthogonal particles consisting of identical components are synthesized successfully via spray-drying, coprecipitation, and solvothermal methods, respectively. The conditions have been optimized to obtain the final samples with controlled morphology and very close surface area (Figure S4 and Table S1). This indicates that the specific surface area of the four samples has a limited impact on the the electrochemical performance of the cathode materials, and it is worthwhile to study the relationship between structure and performance from a new perspective of oxygen vacancy. The morphology and structure information on the four samples are characterized by scanning electron microscopy (SEM). As displayed in Figure 1a and b, the irregular particles have an average grain size between 100 and 200 nm, and the grains have a smooth surface without agglomerations. Different from the irregular particles, microspheres, microrods, and orthogonal particles are uniform microscale secondary particles assembled by nanoscale primary grains in a certain orientation. As shown in Figure 1c and d, the microspheres have a similar diameter of ∼10 μm and are compactly composed of nanosized grains of ∼100 nm. Parts e and f of Figure 1 show that the microrods present a well-arranged rodlike morphology with an approximate length of 8 μm and a diameter of 1−1.5 μm and are composed of grains with a size of 200−300 nm. Moreover, this preferential orientation of the agglomeration mode causes the material to expose more {010} planes that contribute to the diffusion of lithium ions along the *a* or *b* axis in the bulk.[27−29] It is shown in Figure 1g and f that orthogonal microparticles have an overall size of ∼2 μm and are aggregated tightly by nanoscale particles with an average size of 200 nm.

Phase structures of as-prepared cathode materials are identified by powder X-ray diffraction (XRD), as shown in Figure 1i and j. Clearly, the XRD patterns of the four samples can be well-ascribed to the hexagonal α-$NaFeO_2$ structure ($R\overline{3}m$ space group) and monoclinic Li_2MnO_3 structure ($C2/m$ space group).[30−35] The sharp peaks with strong intensity also indicate the good crystallinity of the as-prepared materials. The weak superlattice diffraction peak emerging at $2\theta = 20-25°$ corresponds to the characteristic diffraction peak of the Li_2MnO_3 component, reflecting the orderly arrangement of lithium ions in the transition metal layer forming the MO_6 octahedral superlattice structure.[31,32] Further observation affirms that the superlattice diffraction peaks are classified into (020) and (111) planes of the $C2/m$ space group of monoclinic phase in Figure 1j. It can be seen from the intensity and splitting of the two diffraction peaks that the lithium ions are arranged in an orderly manner in the transition metal layer of the microrod particles. Compared with that of the irregular particles, the (003) diffraction peaks of the microspheres, microrods, and orthorgonal particles shift toward a higher diffraction angle, indicating a shrinkage of the crystal structures. At the same time, the clear splitting of the (018) and (110) peaks also manifests that the as-synthesized cathode materials have an orderly arranged layered structure. The Raman spectra also confirm the layered structures of the four samples in Figure S3 (Supporting Information).

The oxygen vacancy of the Li-rich cathode materials is characterized by electon paramagnetic spectroscopy (EPR) and X-ray photoelectron spectroscopy (XPS). Generally speaking, metal oxides inevitably generate oxygen vacancies on the surface during heat treatment, especially under high-temperature conditions (Figure 2a). In EPR spectra, an oxygen vacancy in metal oxides usually shows a typical signal of *g*-value at 2.00.[14] According to the EPR results, it is revealed in Figure 2b that the concentration of the oxygen vacancies varies with different micro/nanostructures with a descending order: microrods > microspheres > irregular particles > orthogonal

https://dx.doi.org/10.1021/acsami.0c14979

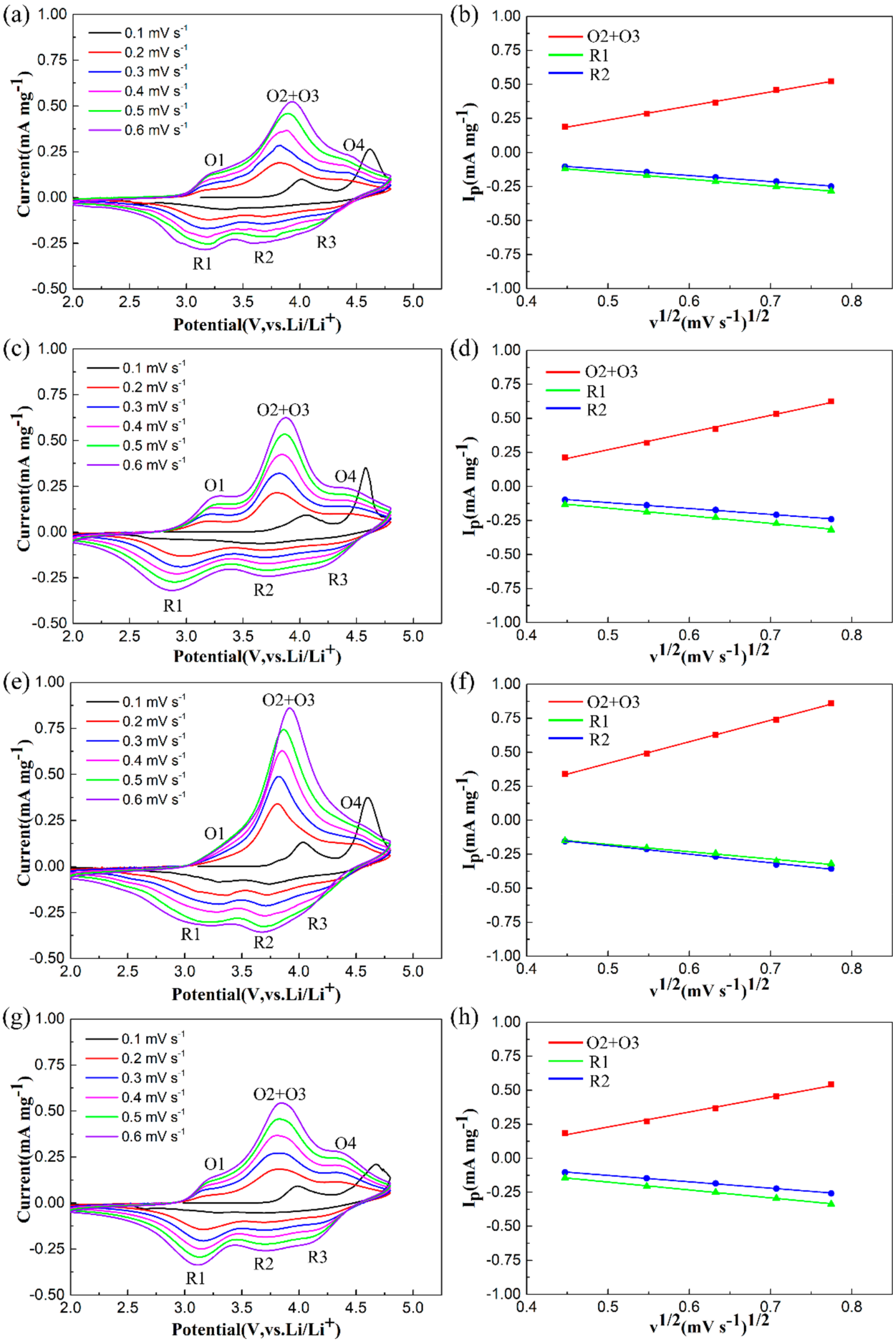

Figure 3. Cyclic voltammograms (CVs) at various scan rates and relationships between peak current and the square root of the scan rate for the specific redox peaks of the irregular particles (a, b), microsphere particles (c, d), microrod particles (e, f), and orthogonal particles (g, h).

particles. The XPS spectra of oxygen are also used to analyze the oxygen vacancies in the different samples. As shown in Figure 2d, the signals at 531.5 and 529.4 eV are ascribed to the oxygen-deficient locations (oxygen vacancies) and lattice oxygen regions (O−M−O), respectively.[36,37] The quantitative analyses based on the XPS peak areas demonstrate that the proportions of oxygen vacancies are 36.5% for microrods, 34.6% for microspheres, 28.9% for irregular particles, and 23.7% for orthogonal particles, which is the same order as the results from EPR. In addition, it can be seen that the average valence state of Ni ions in the microrod particles is slightly lower than that in the other three samples due to the relatively lower binding energy in the Ni 2p spectra (Figure S5, Supporting Information). This is mainly attributed to the abundant oxygen vacancies on the surface of the microrod particles.[5,13] It has been pointed out that oxygen vacancies in Li-rich layered oxides are favorable to lithium-ion diffusion and

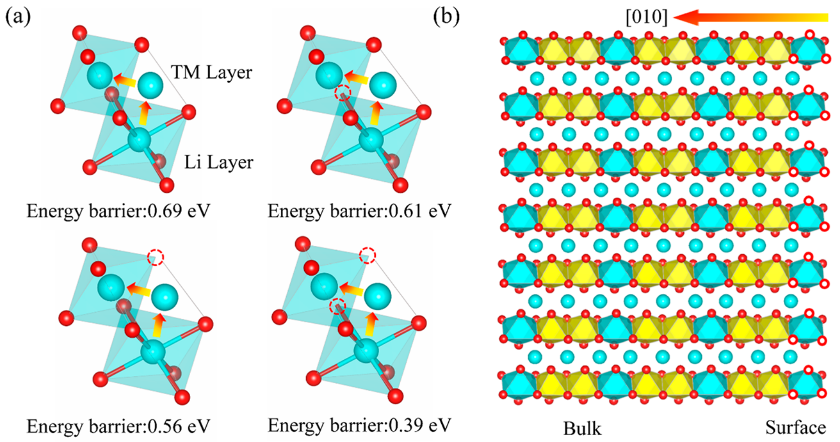

Figure 4. (a) Calculated site stability and energy barriers of no O vacancy, one O vacancy, and two O vacancies in the layered structure. (b) Crystallographic models of the Li_2MnO_3 structure with a surface oxygen vacancy.

helpful for improving electrochemical reactivity and kinetics.[13,23]

To gain more insight into the effect of oxygen vacancies on ion diffusion and the kinetics process of Li-rich cathode materials, cyclic voltametry tests at various scanning rates from 0.1 to 0.6 mV s^{-1} were performed, as shown in Figure 3. Apparently, oxidation (O1) and reduction (R1) peaks at about 3.25 and 3.05 V can be tightly attributed to Mn^{3+} to Mn^{4+} (O1) and Mn^{4+} to Mn^{3+} (R1) redox in the typical layered structure, respectively. What is noteworthy is that no oxidation peaks of Mn^{3+}/Mn^{4+} appear in the initial anodic process among all four samples because all the Mn ions appear tetravalent in the original state. After finishing the first discharge process, Mn^{4+} species are partially reduced to Mn^{3+}, which will persistently exist in the following cycles. It is clear that the O1 oxidation peak of the microrod particles acquires the weakest intensity compared with irregular, microsphere, and orthogonal particles, indicating less active conversion of Mn^{3+}/Mn^{4+} in this specific structure (Figure 3e). On the other hand, trivalent manganese ions are highly susceptible to the Jahn−Teller distortion effect, thereby influencing the structural stability and deteriorating the electrochemical performance.[38] The overlaid oxidation peaks (O2 + O3) that appeared at ~3.85 V are consistent with the $Ni^{2+} \rightarrow Ni^{3+} \rightarrow Ni^{4+}$ (O2) and Co^{3+} to Co^{4+} (O3) multistep processes. Correspondingly, the reduction peaks located at 3.70 and 4.13 V can be ascribed to $Ni^{4+} \rightarrow Ni^{3+} \rightarrow Ni^{2+}$ (R2) and Co^{4+} to Co^{3+} (R3), respectively.[39,40] It is fascinating to note that the peak current of the microrods is significantly higher than the irregular, microsphere, and orthogonal particles in the pair of O2 and R2 regions, which demonstrates that the microrod particles exhibit higher electrochemical reactivity and a more favorable lithium-ion diffusion rate. Additionally, the oxidation peak (O4) is found at ~4.65 V in the first CV curve of the samples. The larger O4 peak is commonly originated from the extraction of Li^+ from the activated Li_2MnO_3 domains under high potential, and the microrod particles exhibit a stronger peak current due to the fast kinetics.[38] At the same time, the O4 peak current of the microrod particles is much weaker than those of the other particles after the first cycle due to the mitigated oxygen-release activity. On the basis of these results, abundant oxygen vacancies of microrod particles on the surface facilitate the lithium-ion intercalation/extraction kinetics in the bulk environment and enhance the cationic electrochemical reactivity.

Besides, in a rate-determined step dominated by the diffusion process, the peak currents at a certain voltage behave as a linear relationship with the square root of the scan rates. Lithium-ion diffusion kinetics in the Li-rich layered oxides can be described by the Randles−Sevick equation,[41]

$$I_p = (2.69 \times 10^5) n^{3/2} A D^{1/2} v^{1/2} C \ (25\ °C)$$

where I_p represents the peak current, n represents the number of electrons transferred in the electrode, A represents the surface area of the active materials, D represents the lithium-ion diffusion coefficient, C represents the concentration of lithium ions, and v represents the scan rate. Because the values of n, A, and C can be regarded as constants in the battery system, the slope of $I_p/v^{1/2}$ reflects the diffusion rate of the lithium ions, which provides important evidence for semi-quantitative analysis of the kinetics in the bulk phase of the cathode materials. The slopes of the O2 + O3, R1, and R2 oxidation/reduction peaks play a crucial role in the electrochemical activity, as shown in Figure 3. Remarkably, the slopes of the O2 + O3 and R2 peaks in the microrod particles are relatively larger compared with irregular, microsphere, and orthogonal particles due to the favorable lithium-ion diffusion path in the specific structure. Meanwhile the slope of the R1 reduction peak assigned to Mn^{4+}/ Mn^{3+} of the microrod particles is the only one less than the slope of the R2 peak among the four samples (Table S2, Supporting Information). The difference results from the stable hierarchical rodlike secondary particles with varying degrees of success, especially suppression of the Jahn−Teller distortion effect triggered by Mn^{3+}. The XPS results of Mn 2p of the microrod particles after 100 cycles, shown in Figure S6 (Supporting Information), also confirm that the average valence state of the Mn element still remains tetravalent and the Jahn−Teller distortion has been effectively controlled.

The mechanism by which oxygen vacancies can promote lithium-ion diffusion can be discussed by the first-principles calculations based on the computational model defined as $Li_{28}Ni_6Mn_{14}O_{48}$, as presented in Figure S7 (Supporting Information) and Figure 4a. In the last stage of discharge, a lithium ion usually migrates from the octahedral site of the lithium layer into the octahedral site of the transition metal layer through an empty tetrahedral site. In the pristine state,

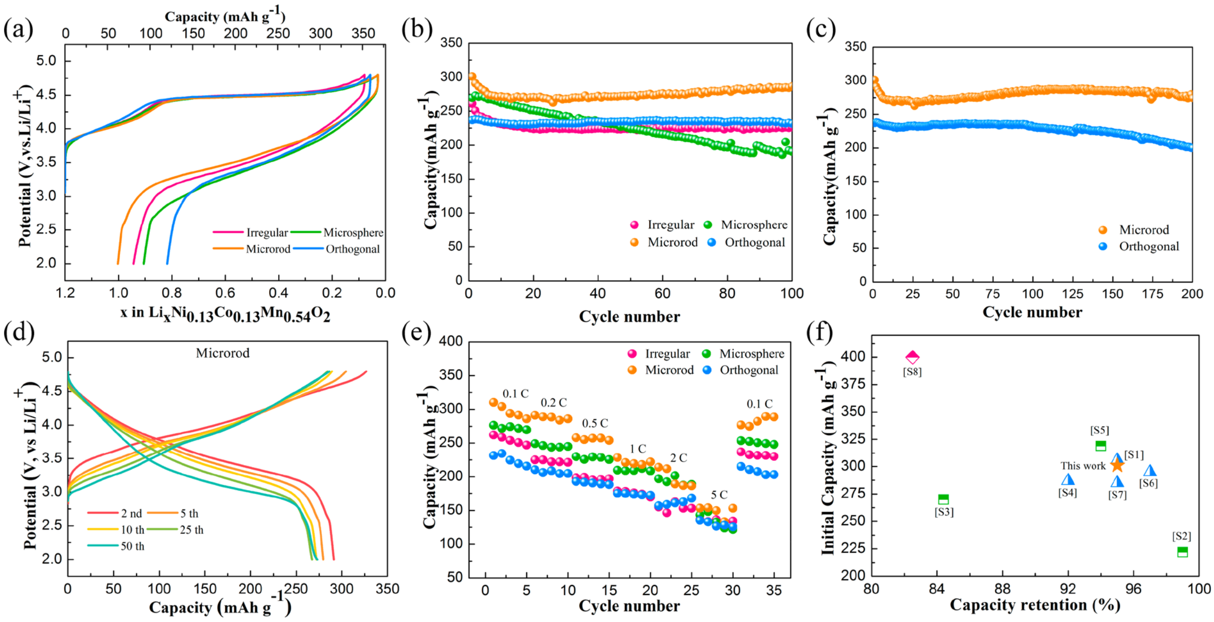

Figure 5. (a) First charge/discharge curves at 0.1C rate. (b, c) Cycling performance at 0.2C rate. (d) Galvanostatic charge/discharge curves from the first cycle to the 50th cycle of the microrod particles. (e) Rate performance. (f) Performance comparison with other works (more detailed information in Table S4, Supporting Information).

the diffusion of the Li ion from the Li layer to the transition metal layer would go through an empty tetrahedral site with an energy barrier of 0.69 eV, which is most stable with no oxygen vacancy. When one oxygen vacancy is introduced, the diffusion energy barriers would be reduced to 0.61 and 0.56 eV, respectively. When two vacancies are introduced at the same time, the diffusion energy barrier would be further decreased to 0.39 eV. The results reveal that the existence of appropriate oxygen vacancies is conducive to the reduction of diffusion energy barriers, promoting the migration of lithium ions. In general, Li-rich layered oxides have a layered hexagonal α-$NaFeO_2$ structure, and Li^+ ions of the lithium layer are preferentially diffused and transported along either the *a*-axis or the *b*-axis. This means that the six equivalent edge planes in the unit cell composed of (010), $(\bar{1}10)$, $(\bar{1}00)$, $(0\bar{1}0)$, $(1\bar{1}0)$, and (100) facets, indexed as {010}, are advantageous and effective planes with an open structure to facilitate lithium ions embedded in the bulk phase, as shown in Figure 4b.[9,26] Oxygen vacancies can accelerate the rapid conduction of lithium ions along the (010) crystal plane by reducing the diffusion energy barrier.

The first galvanostatic charge/discharge profiles of the four samples at 0.1C (1C = 200 mA g^{-1}) are shown in Figures 5a and S8 within the voltage window of 2.0−4.8 V at room temperature. The initial charge curve of the lithium-rich cathode material usually consists of a voltage slope below 4.5 V associated with the oxidation of transition metal cations and a voltage plateau above 4.5 V accompanied by irreversible oxygen loss, which is also the main cause of the low initial Coulombic efficiency.[42,43] The first charge capacities of irregular, microsphere, microrod, and orthogonal particles are 352.4, 367.8, 368.1, and 359.0 mAh g^{-1}, respectively. Correspondingly, the microrod particles deliver the highest discharge capacity of 306.1 mAh g^{-1} compared to those of 271.9 mAh g^{-1} (irregular particles), 275.1 mAh g^{-1} (microsphere particles), and 238.8 mAh g^{-1} (orthogonal particles) at the 0.1C rate. Furthermore, the microrod particles possess the highest initial Coulombic efficiency of 83.2% compared to 77.2% for irregular particles, 74.8% for microsphere particles, and 66.6% for orthogonal particles. Through the first charge/discharge curves, it is found that abundant oxygen vacancies of rod-shaped secondary particles provide a more favorable lithium-ion insertion and extraction channel, thereby supporting a superior discharge capacity. In addition, the surface oxygen vacancies can effectively suppress the irreversible oxygen release under high charge potential, which accounts for the higher initial Coulombic efficiency of the Li-rich cathode materials.[13,18] Moreover, from the structural point of view, the microrod particles are more likely to expose the {010} crystal planes, which greatly facilitates the diffusion of lithium ions and leads to its excellent first cycle performance.[27−29]

Figure 5b displays the cycling performance of the four samples at the 0.2C rate. The initial discharge capacities of irregular particles, microsphere particles, microrod particles, and orthogonal particles are 261.2, 269.7, 301.2, and 237.0 mAh g^{-1}, respectively. After 100 cycles, the microrod particles can hold a discharge capacity of up to 286.6 mAh g^{-1}, much higher than 226 mAh g^{-1} for irregular particles, 190.8 mAh g^{-1} for microsphere particles, and 231.3 mAh g^{-1} for orthogonal particles. The capacity retentions of irregular particles, microsphere particles, microrod particles, and orthogonal particles are 86.7%, 70.8%, 95.2%, and 97.6%, respectively. After 200 cycles, the microrod particles can still keep a higher capacity retention of 91.0%, while the capacity retention of the orthogonal particles is 84.4% in Figure 5c. The superior cyclability of the microrod particles is inseparable from the fast kinetics process and the structural stability. Figures 5d, S9, and S10 show the charge/discharge curves from the first cycle to the 50th cycle of the microrod particles, exhibiting a low declining trend for midpoint voltage. The rate performance of the cathode materials with different morphologies is presented in Figure 5e from 0.1C to 5C. Encouragingly, the microrod particles maintain the best performance among the four

https://dx.doi.org/10.1021/acsami.0c14979
ACS Appl. Mater. Interfaces XXXX, XXX, XXX−XXX

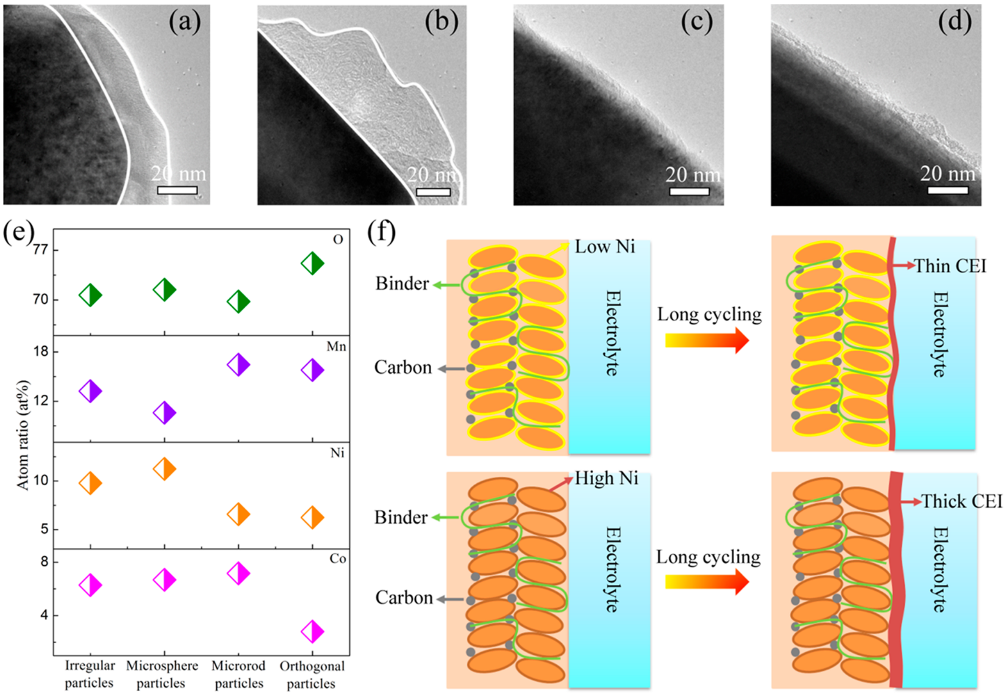

Figure 6. TEM images of (a) irregular particles, (b) microsphere particles, (c) microrod particles, and (d) orthogonal particles after 100 cycles at 0.2C. (e) Atomic ratio results of surface elements measured by XPS full spectra. (f) Illustration of the effect of the surface Ni content on cathode electrolyte interface formation.

samples at all rates and exhibit a discharge capacity of ~280 mAh g^{-1} when the rate recovers from 5C to 0.1C. As compared with previous works adopting strategies of coating, doping, and novel structures in recent years, the microrod particles have also shown relatively excellent electrochemical properties, as listed in Figure 5f. In summary, the microrod particles with rich oxygen vacancies obtain a higher discharge capacity and a better rate performance compared with other cathode materials.

Figure 6 discloses the transmission electron microscopy (TEM) images of cathode materials with different morphologies after 100 cycles. From Figure 6a, a layer with a thickness of ~20 nm can be found on the surface of the irregular particles, which is known as a cathode electrolyte interface (CEI) film. Figure 6b shows that a thicker and more uneven CEI film with a thickness of up to 50 nm is formed on the microsphere particles. A smooth surface without an obvious film is found on the cycled microrod particles, and the thickness of the uniform film found on the orthogonal particles is just ~5 nm, as shown in Figure 6c and d. Usually, the formation of a CEI film is related to a higher nickel content on the surface of the cathode materials.[3,8] In the highly delithiated state, complicated interactions are prone to occur between Ni^{4+} ions and the electrolyte, and they even cause decomposition of the electrolyte.[3,44,45] The atomic ratio results of the surface elements measured by XPS full spectra are summarized in Figure 6e. The generation of oxygen vacancies leads to the uneven distribution of transition metal ions on the surface of the cathode particle.[18] It is clear that microsphere particles exhibit higher Ni content and lower Mn content on the surface, which is distinct from irregular, microrod, and orthogonal particles. Higher nickel content contributes to forming a thick CEI film on the surface, while lower Mn content is harmful to the thermal stability of microsphere particles.[8] Although the relatively abundant oxygen vacancies of the microsphere particles provide them with a high initial discharge capacity, the higher nickel content on the surface causes serious side reactions and leads to a thicker CEI film during cycling. It also explains why microsphere particles exhibit the worst cycling performance. These results are summarized in Figure 6f, in which the illustration demonstrates the effect of the surface Ni content on CEI formation.

The electrochemical impedance spectra (EIS) of cathode materials with different morphologies fully charged to 4.8 V are conducted to evaluate the effect of structure control on the electrochemical properties after the first cycle and the 100th cycle. The fitted equivalent circuit is presented in Figure 7e, and the fitted data is summarized in Table S3. The semicircles in the Nyquist plots represent the resistance and capacitance of the electrolyte interface film of the cathode named the surface charge-transfer resistance (Rct).[44] After the activation in the first charge at the 0.1C rate, the microrod particles get the lowest Rct value among the four samples, which is consistent with the cell using microrod particles delivering the highest discharge capacity in the first cycle. The larger Rct value in the first cycle of the Li-rich layered oxides is closely related to the complicated formation process of the cathode electrolyte interface (CEI) film. After 100 cycles, the microrod particles still hold the minimum Rct value compared with the irregular, microsphere, and orthogonal particles. This is because the rodlike structure has a rapid lithium-ion diffusion rate and enhanced electron conductivity with a thin and stable CEI film. In response, the fine intrinsic surface structure with rich oxygen vacancies results in the desirable cycling and rate performance.[46−48] Meanwhile, the microsphere particles acquire the maximum Rct value of up to 349 Ω after 100 cycles, which explains the weak cycle performance.

As for further investigation on the microstructure and phase composition, high-resolution transmission electron microscopy (HRTEM) examinations of all the as-prepared samples are

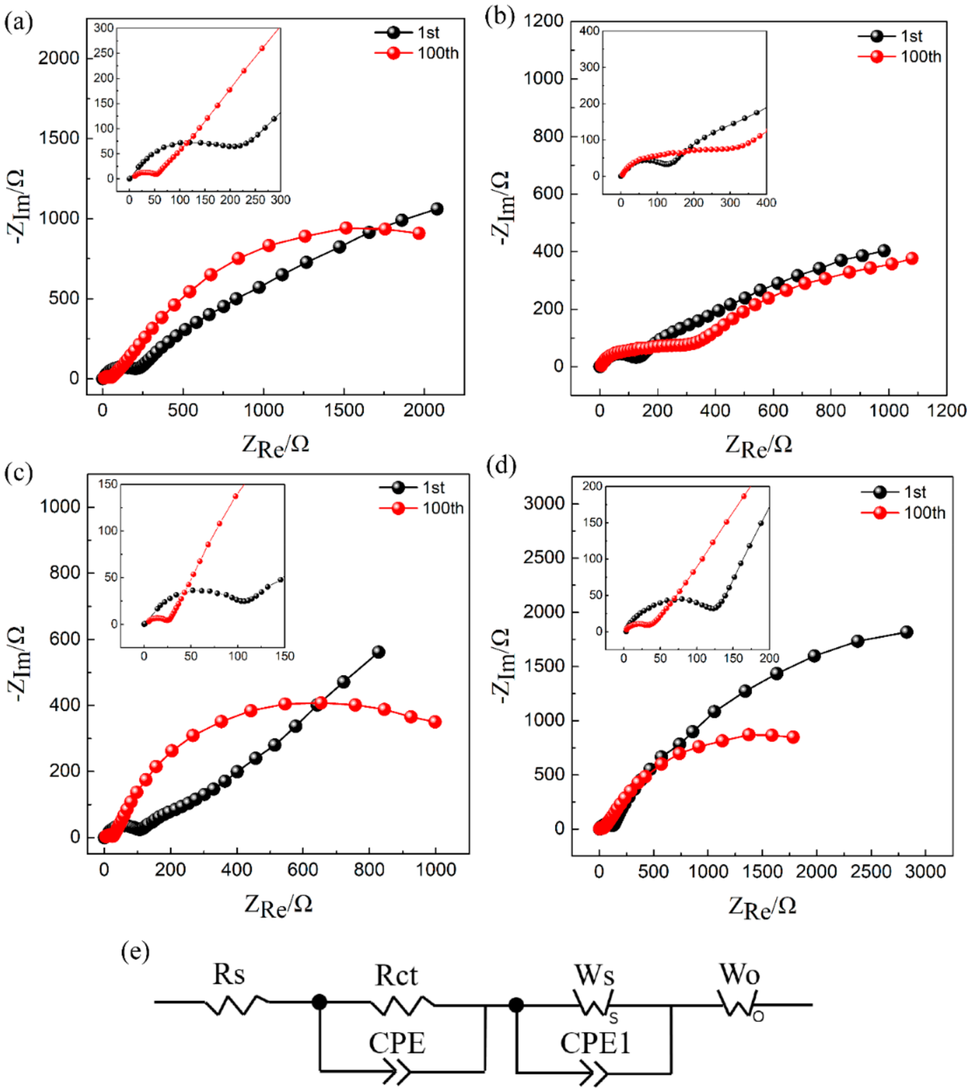

Figure 7. EIS results of irregular (a), microsphere (b), microrod (c), and orthogonal particles (d) after different cycles at the fully charged state at 1C rate and equivalent circuit (e) employed to fit the obtained data.

shown in Figure S11 (Supporting Information), and the results of the microrod particles before and after cycling are shown in Figure 8. It is revealed in Figure 8a and b that the pristine microrod particles have an explicit, well-defined, layered α-$NaFeO_2$ structure with a hexagonal R$\bar{3}$ m phase, in which two sets of lattice fringes of 0.47 and 0.24 nm can be indexed to the (003) and (101) crystal planes. The selected area electron diffraction (SAED) result confirms the layered structure of the pristine microrod particles with consistent results. Figure 8c displays the scanning transmission electron microscopy (STEM) image of the microrod particles after 200 cycles without any cracks. The line-scan results of the single particle (cyan zone) in Figure 8d uncover that the nickel, cobalt, and manganese elements are uniformly distributed on the surface and center of the particle even after 200 cycles, which has no significant difference with the distribution of transition metal cations in the pristine particle (Figure S2, Supporting Information). Analysis of the structural transformation during cycling is employed on the cycled microrod particles (taken from the yellow zone in Figure 8c). The cycled microrod particles still maintain a stable layered structure with a typical lattice fringe of 0.47 nm assigned to the (003) plane through the HRTEM and SAED in Figure 8e. It is obvious that the rodlike structure enables suppression of the phase transformation from layered to spinel or even rock-salt phase over cycling. In addition, a thin cathode electrolyte interface (CEI) film is formed on the surface of the microrod particles with a thickness of <1 nm, which is attributed to the mitigated interfacial side reactions. On the contrary, the microsphere particles appear to have obvious cracks after 100 cycles that are closely related to the serious structural transformation and structural instability during cycling, as shown in Figure S12 (Supporting Information). TEM energy-dispersive X-ray spectroscopy (TEM-EDS) mappings also verify the uniform distribution of transition metal cations in the microrod particles even after long cycling.

3. CONCLUSION

In summary, irregular, microsphere, microrod, and orthogonal particles are successfully synthesized under the control of micro/nanostructures. The contents of the oxygen vacancies generated on the surface are clarified to vary with different morphologies. On the basis of the comparative analysis, it is clear that an intrinsic oxygen vacancy plays an essential role in

https://dx.doi.org/10.1021/acsami.0c14979

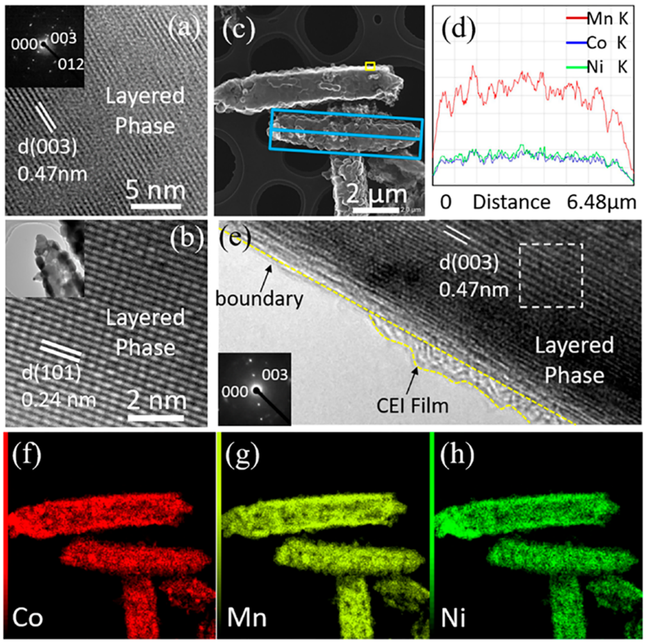

Figure 8. (a, b) HRTEM images and SAED pattern of microrod particles before cycling. (c−e) STEM image, corresponding line-scan results, HRTEM image, SAED pattern, and (f−h) EDS mappings of Co, Mn, and Ni of the microrod particles after 200 cycles at 0.2C.

increasing the electrochemical performance of Li-rich cathode materials. Basically, oxygen vacancies can accelerate the rapid conduction of lithium ions along the (010) crystal plane by reducing the diffusion energy barrier. Moreover, oxygen vacancies can effectively suppress the Jahn−Teller distortion effect, thereby effectively improving the structural stability. In addition, phase transformation from layered to spinel structures is also markedly alleviated in the cycled microrods with a thin CEI film. As a result, microrod particles with abundant oxygen vancancies deliver a discharge capacity of 306.1 mAh g^{-1} at 0.1C with an initial Coulombic efficiency of 83.2%, and they also obtain the most excellent cycling and rate performance compared with irregular, microsphere, and orthogonal particles. It can be inferred that the premeditated micro/nanostructure enables the rational synthesis of energy storage materials and that abundant oxygen vacancies are capable of achieving higher energy and power density.

4. EXPERIMENTAL SECTION

4.1. Preparation of Irregular Particles. A stoichiometric ratio of $LiOH{\cdot}H_2O$ (5% excess), $(CH_3COO)_2Ni{\cdot}4H_2O$, $(CH_3COO)_2Mn{\cdot}4H_2O$, and $(CH_3COO)_2Co{\cdot}4H_2O$ was added to deionized water and mixed together with a total metal cation concentration of 0.5 mol/L. Citric acid was dissolved in 150 mL of deionized water and then pumped into the earlier-described suspension at a 2 mL/min rate. Then ammonia was applied to adjust the pH to 9. The solution was pumped into a spray dryer at 120 °C to obtain precursors. The precursors were pretreated at 480 °C for 5 h and finally calcined at 850 °C for 10 h to obtain the cathode materials under air atmosphere.

4.2. Preparation of Microsphere Particles. A stoichiometric ratio of $CoSO_4{\cdot}7H_2O$, $MnSO_4{\cdot}H_2O$, and $NiSO_4{\cdot}6H_2O$ was added into 1 L of deionized water with a metal ion concentration of 2 M. Na_2CO_3 and 30 mL of $NH_3{\cdot}H_2O$ were added into deionized water to gain 2 L of buffer solution. Then a certain amount of ultrapure water was added to the reaction vessel and heated to 50 °C with stirring. The salt solution and the alkali solution were separately added to the reaction vessel to control the pH to 8.6, and the precursors were obtained after filtration and drying. After grinding with Li_2CO_3 (5% excess) in a stoichiometric ratio, it was calcined at 600 °C for 4 h and then at 850 °C for 10 h in the muffle furnace to obtain microsphere particles.

4.3. Preparation of Microrod Particles. Stoichiometric amounts of $CH_3COOLi{\cdot}H_2O$ (5% excess), $(CH_3COO)_2Mn{\cdot}4H_2O$, $(CH_3COO)_2Co{\cdot}4H_2O$, and $(CH_3COO)_2Ni{\cdot}4H_2O$ were dissolved into a mixed solution containing 10 mL of ultrapure water and 10 mL of ethanol. Oxalic acid (0.12 mol) was dissolved into 80 mL of ethanol and mixed well with the metal salt solution. Then the solution was transferred to a polytetrafluoroethylene autoclave and reacted at 180 °C for 12 h. The obtained precursors were filtered and dried at 60 °C overnight. Next, the precursors were pretreated at 450 °C for 6 h and treated at 900 °C for 12 h in air to obtain microrod particles.

4.4. Preparation of Orthogonal Particles. Hexamethylenetetramine (1.06 g) was added to 25 mL of ultarpure water and then dissolved with a stoichiometric ratio of $(CH_3COO)_2Mn{\cdot}4H_2O$, $(CH_3COO)_2Co{\cdot}4H_2O$, and $(CH_3COO)_2Ni{\cdot}4H_2O$ with stirring for 2 h. Ethanol (10 mL) was added into the solution and stirred continuously for 10 min. Next the solution was transferred to a Teflon autoclave and treated at 160 °C for 24 h at a heating rate of 3 °C/min. After vacuum-drying at 80 °C for 12 h, the precursors were calcined at 450 °C for 5 h at air. Finally, the oxide precursors were ground with $LiOH{\cdot}H_2O$ (5% excess) and calcined at 800 °C for 12 h in the muffle furnace to obtain orthogonal particles.

4.5. Material Characterization. The phase structure was detected by X-ray powder diffraction (XRD, Bruker D8 FOCUS) with a range of $2\theta = 10{-}80°$. SEM (JEOL-7800F) and corresponding EDS, TEM (JEOL-JEM2800), and HRTEM were used to obtain the morphologies, elemental distribution, and lattice fringes, respectively. The EPR spectra were obtained on a JES-FA 200 EPR spectrometer. An X-ray photoelectron spectrometer (Thermo Scientific ESCALAB 250Xi) was utilized to gain the information on the element chemical state. Raman spectroscopy was employed at a 532 nm excitation wavelength with a SR-500I-A Raman spectrometer.

4.6. Electrochemical Test. The slurry composed of 80 wt % pristine cathode materials, 10 wt % Super P, 10 wt % polyvinylidene fluoride (PVDF), and *N*-methylpyrrolidone (NMP) solution as a dispersant was coated on Al foil and dried at 110 °C overnight. The electrolyte was composed of $LiPF_6$ (1 M) in a mixed solvent of ethylene carbonate (EC) and dimethyl carbonate (DMC) with a volume ratio of 3:7. CR2032-type half-coin cells were installed in an Ar-filled glovebox with lithium as the anode and tested on a LAND-CT2001A tester. The cyclic voltammograms (CVs) were conducted by an electrochemical workstation (CHI 600E, Shanghai Chenhua) at different scan rates (0.1−0.6 mV s^{-1}). Electrochemical impedance spectra (EIS) were performed at the full-charged state of 4.8 V on an electrochemical workstation (Vertex V16429) that ranged from 10 mHz to 100 kHz.

4.7. Computation Methodology. In this work, first-principles calculations on the basis of spin-polarized density function theory (DFT) were implemented with the plane-wave technique as performed in the Vienna ab initio simulation package (VASP).[49] The projector augmented wave (PAW) method was applied to demonstrate the ion−electron interaction.[50] The plane wave basis set selected a 450 eV cutoff. Considering the strong electron correlation effects, the calculations involving Mn were performed at the DFT + U level with a U value of 5 eV, which is consistent with previous reports.[51] The generalized gradient approximation (GGA) in the form of Perdew, Burke, and Ernzerhof (PBE) was applied to demonstrate exchange-correlation energy.[52] The Brillouin zones were sampled with 6 × 3 × 6 Monkhorst−Pack meshes.[53] The minimum-energy path and diffusion barriers for Li inside Li_2MnO_3 were studied via the climbing-image nudged elastic band (CI-NEB) method.[54]

■ ASSOCIATED CONTENT

Supporting Information

The Supporting Information is available free of charge at https://pubs.acs.org/doi/10.1021/acsami.0c14979.

Schematic diagram of the synthesis path, SEM-EDS line scan results, Raman spectroscopy, BET results, XPS spectra of transition metal elements, midpoint voltage curves, TEM images of the pristine cathode material, and SEM images of the cycled cathode material (PDF)

AUTHOR INFORMATION

Corresponding Author

Guo-Ran Li − *Institute of New Energy Material Chemistry, School of Materials Science and Engineering, Renewable Energy Conversion and Storage Center, Nankai University, Tianjin 300350, P. R. China;* orcid.org/0000-0002-6380-5725; Phone: +86-22-23500780; Email: guoranli@nankai.edu.cn

Authors

Shao-Lun Cui − *Institute of New Energy Material Chemistry, School of Materials Science and Engineering, Renewable Energy Conversion and Storage Center, Nankai University, Tianjin 300350, P. R. China*

Xu Zhang − *Institute of New Energy Material Chemistry, School of Materials Science and Engineering, Renewable Energy Conversion and Storage Center, Nankai University, Tianjin 300350, P. R. China*

Xue-Wen Wu − *Institute of New Energy Material Chemistry, School of Materials Science and Engineering, Renewable Energy Conversion and Storage Center, Nankai University, Tianjin 300350, P. R. China*

Sheng Liu − *Institute of New Energy Material Chemistry, School of Materials Science and Engineering, Renewable Energy Conversion and Storage Center, Nankai University, Tianjin 300350, P. R. China;* orcid.org/0000-0001-5933-1101

Zhen Zhou − *Institute of New Energy Material Chemistry, School of Materials Science and Engineering, Renewable Energy Conversion and Storage Center, Nankai University, Tianjin 300350, P. R. China;* orcid.org/0000-0003-3232-9903

Xue-Ping Gao − *Institute of New Energy Material Chemistry, School of Materials Science and Engineering, Renewable Energy Conversion and Storage Center, Nankai University, Tianjin 300350, P. R. China;* orcid.org/0000-0001-7305-7567

Complete contact information is available at:
https://pubs.acs.org/10.1021/acsami.0c14979

Notes

The authors declare no competing financial interest.

ACKNOWLEDGMENTS

This work was supported by the National Key Research and Development Program (2016YFB0100200). The authors greatly thank the financial fund from Natural Science Foundation of Tianjin (18JCZDJC31000).

REFERENCES

(1) Tarascon, J. M.; Armand, M. Issues and Challenges Facing Rechargeable Lithium Batteries. *Nature* **2001**, *414*, 359−367.

(2) Huang, G.; Han, J. H.; Lu, Z.; Wei, D. X.; Kashani, H.; Watanabe, K.; Chen, M. W. Ultrastable Silicon Anode by Three-Dimensional Nanoarchitecture Design. *ACS Nano* **2020**, *14*, 4374−4382.

(3) You, Y.; Celio, H.; Li, J. Y.; Dolocan, A.; Manthiram, A. Modified High-Nickel Cathodes with Stable Surface Chemistry Against Ambient Air for Lithium-Ion Batteries. *Angew. Chem., Int. Ed.* **2018**, *57*, 6480−6485.

(4) Zhao, Y.; Liu, J. T.; Wang, S. B.; Ji, R.; Xia, Q. B.; Ding, Z. P.; Wei, W. F.; Liu, Y.; Wang, P.; Ivey, D. G. Surface Structural Transition Induced by Gradient Polyanion-Doping in Li-Rich Layered Oxides: Implications for Enhanced Electrochemical Performance. *Adv. Funct. Mater.* **2016**, *26*, 4760−4767.

(5) Wu, B.; Yang, X. K.; Jiang, X.; Zhang, Y.; Shu, H. B.; Gao, P.; Liu, L.; Wang, X. Y. Tailoring Surface Structure and Chemical Composition of Li-Rich-Layered Oxide for High-Energy Lithium-Ion Batteries. *Adv. Funct. Mater.* **2018**, *28*, 1803392.

(6) Zuo, Y. X.; Li, B.; Jiang, N.; Chu, W. S.; Zhang, H.; Zou, R. Q.; Xia, D. G. A High-Capacity O2-Type Li-Rich Cathode Material with a Single-Layer Li$_2$MnO$_3$ Superstructure. *Adv. Mater.* **2018**, *30*, 1707255.

(7) Wang, J.; He, X.; Paillard, E.; Laszczynski, N.; Li, J.; Passerini, S. Lithium- and Manganese-Rich Oxide Cathode Materials for High-Energy Lithium Ion Batteries. *Adv. Energy Mater.* **2016**, *6*, 1600906.

(8) Sathiya, M.; Abakumov, A. M.; Foix, D.; Rousse, G.; Ramesha, K.; Saubanère, M.; Doublet, M. L.; Vezin, H.; Laisa, C. P.; Prakash, A. S.; et al. Origin of Voltage Decay in High-Capacity Layered Oxide Electrodes. *Nat. Mater.* **2015**, *14*, 230.

(9) Xu, M.; Fei, L. F.; Zhang, W. B.; Li, T.; Lu, W.; Zhang, N.; Lai, Y. Q.; Zhang, Z. A.; Fang, J.; Zhang, K.; Li, J.; Huang, H. T. Tailoring Anisotropic Li-Ion Transport Tunnels on Orthogonally Arranged Li-Rich Layered Oxide Nanoplates Toward High-Performance Li-Ion Batteries. *Nano Lett.* **2017**, *17*, 1670−1677.

(10) Gu, M.; Belharouak, I.; Zheng, J. M.; Wu, H. M.; Xiao, J.; Genc, A.; Amine, K.; Thevuthasan, S.; Baer, D. R.; Zhang, J. G.; Browning, N. D.; Liu, J.; Wang, C. M. Formation of the Spinel Phase in the Layered Composite Cathode Used in Li-Ion Batteries. *ACS Nano* **2013**, *7*, 760−767.

(11) Trogadas, P.; Ramani, V.; Strasser, P.; Fuller, T. F.; Coppens, M. O. Hierarchically Structured Nanomaterials for Electrochemical Energy Conversion. *Angew. Chem., Int. Ed.* **2016**, *55*, 122−148.

(12) Song, H. K.; Lee, K. T.; Kim, M. G.; Nazar, L. F.; Cho, J. Recent Progress in Nanostructured Cathode Materials for Lithium Secondary Batteries. *Adv. Funct. Mater.* **2010**, *20*, 3818−3834.

(13) Ma, Y. T.; Liu, P. F.; Xie, Q. S.; Zhang, G. B.; Zheng, H. F.; Cai, Y. X.; Li, Z.; Wang, L. S.; Zhu, Z. Z.; Mai, L. Q.; Peng, D. L. Double-Shell Li-Rich Layered Oxide Hollow Microspheres with Sandwich-Like Carbon@ Spinel@ Layered@ Spinel@ Carbon Shells as High-Rate Lithium Ion Battery Cathode. *Nano Energy* **2019**, *59*, 184−196.

(14) Wang, Z.; Lin, X. Y.; Zhang, J. T.; Wang, D.; Ding, C. Y.; Zhu, Y. M.; Gao, P.; Huang, X. X.; Wen, G. W. Spherical Layered Li-Rich Cathode Material: Unraveling the Role of Oxygen Vacancies on Improving Lithium Ion Conductivity. *J. Power Sources* **2020**, *462*, 228171.

(15) Zhou, L.; Zhao, D.; Lou, X. LiNi$_{0.5}$Mn$_{1.5}$O$_4$ Hollow Structures as High-Performance Cathodes for Lithium-Ion Batteries. *Angew. Chem., Int. Ed.* **2012**, *51*, 239−241.

(16) Oishi, M.; Yamanaka, K.; Watanabe, I.; Shimoda, K.; Matsunaga, T.; Arai, H.; Ukyo, Y.; Uchimoto, Y.; Ogumi, Z.; Ohta, T. Direct Observation of Reversible Oxygen Anion Redox Reaction in Li-Rich Manganese Oxide, Li$_2$MnO$_3$, Studied by Soft X-ray Absorption Spectroscopy. *J. Mater. Chem. A* **2016**, *4*, 9293−9302.

(17) Armstrong, R. A.; Holzapfel, M.; Novák, P.; Johnson, C. S.; Kang, S. H.; Thackeray, M. M.; Bruce, P. G. Demonstrating Oxygen Loss and Associated Structural Reorganization in the Lithium Battery Cathode Li[Ni$_{0.2}$Li$_{0.2}$Mn$_{0.6}$]O$_2$. *J. Am. Chem. Soc.* **2006**, *128*, 8694−8698.

(18) Nakamura, T.; Gao, T. Z.; Ohta, K.; Kimura, Y.; Tamenori, Y.; Nitta, K.; Ina, T.; Oishi, M.; Amezawa, K. Defect Chemical Studies on Oxygen Release from the Li-Rich Cathode Material Li$_{1.2}$Mn$_{0.6}$Ni$_{0.2}$O$_{2-\delta}$. *J. Mater. Chem. A* **2019**, *7*, 5009−5019.

(19) Goodenough, J. B.; Kim, Y. Challenges for Rechargeable Li Batteries. *Chem. Mater.* **2010**, *22*, 587−603.

(20) Zhang, N.; Cheng, F.; Liu, J.; Wang, L.; Long, X.; Liu, X.; Li, F.; Chen, J. Rechargeable Aqueous Zinc-Manganese Dioxide Batteries with High Energy and Power Densities. *Nat. Commun.* **2017**, *8*, 405.

(21) Giordano, L.; Karayaylali, P.; Yu, Y.; Katayama, Y.; Maglia, F.; Lux, S.; Shao-Horn, Y. Chemical Reactivity Descriptor for the Oxide-

Electrolyte Interface in Li-Ion Batteries. *J. Phys. Chem. Lett.* **2017**, *8*, 3881.

(22) Kong, F. T.; Liang, C. P.; Wang, L. H.; Zheng, Y. P.; Perananthan, S.; Longo, R. C.; Ferraris, J. P.; Kim, M.; Cho, K. Kinetic Stability of Bulk $LiNiO_2$ and Surface Degradation by Oxygen Evolution in $LiNiO_2$-Based Cathode Materials. *Adv. Energy Mater.* **2019**, *9*, 1802586.

(23) Fang, G. Z.; Zhu, C. Y.; Chen, M. H.; Zhou, J.; Tang, B. Y.; Cao, X. X.; Zheng, X. S.; Pan, A. Q.; Liang, S. Q. Suppressing Manganese Dissolution in Potassium Manganate with Rich Oxygen Defects Engaged High-Energy-Density and Durable Aqueous Zinc-Ion Battery. *Adv. Funct. Mater.* **2019**, *29*, 1808375.

(24) Tan, X.; Liu, R.; Xie, C.; Shen, Q. Modified Structural Characteristics and Enhanced Electrochemical Properties of Oxygen-Deficient $Li_2MnO_{3-\delta}$ Obtained from Pristine Li_2MnO_3. *J. Power Sources* **2018**, *374*, 134−141.

(25) Fu, F.; Yao, Y. Z.; Wang, H. Y.; Xu, G. L.; Amine, K.; Sun, S. G.; Shao, M. H. Structure Dependent Electrochemical Performance of Li-Rich Layered Oxides in Lithium-Ion Batteries. *Nano Energy* **2017**, *35*, 370−378.

(26) Manthiram, A.; Knight, J. C.; Myung, S. T.; Oh, S. M.; Sun, Y. K. Nickel-Rich and Lithium-Rich Layered Oxide Cathodes: Progress and Perspectives. *Adv. Energy Mater.* **2016**, *6*, 1501010.

(27) Wei, G. Z.; Lu, X.; Ke, F. S.; Huang, L.; Li, J. T.; Wang, Z. X.; Zhou, Z. Y.; Sun, S. G. Crystal Habit-Tuned Nanoplate Material of $Li[Li_{1/3-2x/3}Ni_xMn_{2/3-x/3}]O_2$ for High-Rate Performance Lithium-Ion Batteries. *Adv. Mater.* **2010**, *22*, 4364−4367.

(28) Chen, L.; Su, Y. F.; Chen, S.; Li, N.; Bao, L. Y.; Li, W. K.; Wang, Z.; Wang, M.; Wu, F. Hierarchical $Li_{1.2}Ni_{0.2}Mn_{0.6}O_2$ Nanoplates with Exposed {010} Planes as High-Performance Cathode Material for Lithium-Ion Batteries. *Adv. Mater.* **2014**, *26*, 6756−6760.

(29) Fu, F.; Xu, G. L.; Wang, Q.; Deng, Y. P.; Li, X.; Li, J. T.; Huang, L.; Sun, S. G. Synthesis of Single Crystalline Hexagonal Nanobricks of $LiNi_{1/3}Co_{1/3}Mn_{1/3}O_2$ with High Percentage of Exposed {010} Active Facets as High Rate Performance Cathode Material for Lithium-Ion Battery. *J. Mater. Chem. A* **2013**, *1*, 3860−3864.

(30) Yang, X. K.; Wang, D.; Yu, R. Z.; Bai, Y. S.; Shu, H. B.; Ge, L.; Guo, H. P.; Wei, Q. L.; Liu, L.; Wang, X. Y. Suppressed Capacity/Voltage Fading of High-Capacity Lithium-Rich Layered Materials via the Design of Heterogeneous Distribution in the Composition. *J. Mater. Chem. A* **2014**, *2*, 3899−3911.

(31) Luo, K.; Roberts, M. R.; Guerrini, N.; Tapia-Ruiz, N.; Hao, R.; Massel, F.; Pickup, D. M.; Ramos, S.; Liu, Y. S.; Guo, J. H.; Chadwick, A. V.; Duda, L. C.; Bruce, P. G. Anion Redox Chemistry in the Cobalt Free 3d Transition Metal Oxide Intercalation Electrode $Li[Li_{0.2}Ni_{0.2}Mn_{0.6}]O_2$. *J. Am. Chem. Soc.* **2016**, *138*, 11211−11218.

(32) Rozier, P.; Tarascon, J. M. Li-Rich Layered Oxide Cathodes for Next-Generation Li-Ion Batteries: Chances and Challenges. *J. Electrochem. Soc.* **2015**, *162*, A2490−A2499.

(33) Hong, J.; Seo, D.-H.; Kim, S. W.; Gwon, H.; Oh, S. T.; Kang, K. Structural Evolution of Layered $Li_{1.2}Ni_{0.2}Mn_{0.6}O_2$ upon Electrochemical Cycling in a Li Rechargeable Battery. *J. Mater. Chem.* **2010**, *20*, 10179−10186.

(34) Venkateswara Rao, C.; Leela Mohana Reddy, A.; Ishikawa, Y.; Ajayan, P. M. $LiNi_{1/3}Co_{1/3}Mn_{1/3}O_2$-Graphene Composite as a Promising Cathode for Lithium-Ion Batteries. *ACS Appl. Mater. Interfaces* **2011**, *3*, 2966−2972.

(35) Amalraj, F.; Kovacheva, D.; Talianker, M.; Zeiri, L.; Grinblat, J.; Leifer, N.; Goobes, G.; Markovsky, B.; Aurbach, D. Synthesis of Integrated Cathode Materials $xLi_2MnO_3\cdot(1-x)\ LiMn_{1/3}Ni_{1/3}Co_{1/3}O_2$ (x= 0.3, 0.5, 0.7) and Studies of Their Electrochemical Behavior. *J. Electrochem. Soc.* **2010**, *157*, A1121−A1130.

(36) Zeng, Y.; Lai, Z.; Han, Y.; Zhang, H.; Xie, S.; Lu, X. Oxygen-Vacancy and Surface Modulation of Ultrathin Nickel Cobaltite Nanosheets as a High-Energy Cathode for Advanced Zn-Ion Batteries. *Adv. Mater.* **2018**, *30*, 1802396.

(37) Zhao, J. Q.; Huang, R. M.; Gao, W. P.; Zuo, J. M.; Zhang, X. F.; Misture, S. T.; Chen, Y.; Lockard, J. V.; Zhang, B. L.; Guo, S. M.; Khoshi, M. R.; Dooley, K.; He, H. X.; Wang, Y. An Ion-Exchange Promoted Phase Transition in a Li-Excess Layered Cathode Material for High-Performance Lithium Ion Batteries. *Adv. Energy Mater.* **2015**, *5*, 1401937.

(38) Pang, S. L.; Zhu, M.; Xu, K. J.; Shen, X. Q.; Wen, H. R.; Su, Y. J.; Yang, G. M.; Wu, X.; Li, S. W.; Wang, W. Z.; Xi, X. M.; Wang, H. B. Enhanced Electrochemical Performance of $Li_{1.2}Mn_{0.54}Ni_{0.13}Co_{0.13}O_2$ via L-Ascorbic Acid-Based Treatment as Cathode Material for Li-Ion batteries. *J. Electrochem. Soc.* **2018**, *165*, A1897−A1902.

(39) Ates, M. N.; Mukerjee, S.; Abraham, K. M. A Li-Rich Layered Cathode Material with Enhanced Structural Stability and Rate Capability for Li-Ion Batteries. *J. Electrochem. Soc.* **2014**, *161*, A355−A363.

(40) Yu, H. J.; Kim, H.; Wang, Y. R.; He, P.; Asakura, D.; Nakamura, Y.; Zhou, H. S. High-Energy 'Composite' Layered Manganese-Rich Cathode Materials via Controlling $Li_2\ MnO_3$ Phase Activation for Lithium-Ion Batteries. *Phys. Chem. Chem. Phys.* **2012**, *14*, 6584−6595.

(41) Liu, Y. T.; Han, D. D.; Wang, L.; Li, G. R.; Liu, S.; Gao, X. P. $NiCo_2O_4$ Nanofibers as Carbon-Free Sulfur Immobilizer to Fabricate Sulfur-Based Composite with High Volumetric Capacity for Lithium-Sulfur Battery. *Adv. Energy Mater.* **2019**, *9*, 1803477.

(42) Luo, K.; Roberts, M. R.; Hao, R.; Guerrini, N.; Pickup, D. M.; Liu, Y. S.; Edström, K.; Guo, J.; Chadwick, A. V.; Duda, L. C.; Bruce, P. G. Charge-Compensation in 3d-Transition-Metal-Oxide Intercalation Cathodes Through the Generation of Localized Electron Holes on Oxygen. *Nat. Chem.* **2016**, *8*, 684.

(43) Ye, D.; Zeng, G.; Nogita, K.; Ozawa, K.; Hankel, M.; Searles, D. J.; Wang, L. Understanding the Origin of Li_2MnO_3 Activation in Li-Rich Cathode Materials for Lithium-Ion Batteries. *Adv. Funct. Mater.* **2015**, *25*, 7488−7496.

(44) Zuo, X. X.; Fan, C. J.; Liu, J. S.; Xiao, X.; Wu, J. H.; Nan, J. M. Effect of Tris (trimethylsilyl) borate on the High Voltage Capacity Retention of $LiNi_{0.5}Co_{0.2}Mn_{0.3}O_2$/Graphite Cells. *J. Power Sources* **2013**, *229*, 308−312.

(45) Hua, W. B.; Chen, M. Z.; Schwarz, B.; Knapp, M.; Bruns, M.; Barthel, J.; Yang, X. S.; Sigel, F.; Azmi, R.; Senyshyn, A.; Missiul, A.; Simonelli, L.; Etter, M.; Wang, S. N.; Mu, X. K.; Fiedler, A.; Binder, J. R.; Guo, X. D.; Chou, S. L.; Zhong, B.; Indris, S.; Ehrenberg, H. Lithium/Oxygen Incorporation and Microstructural Evolution during Synthesis of Li-Rich Layered $Li[Li_{0.2}Ni_{0.2}Mn_{0.6}]O_2$ Oxides. *Adv. Energy Mater.* **2019**, *9*, 1803094.

(46) Zheng, M. T.; Xing, C.; Zhang, W. P.; Cheng, Z. L.; Liu, X. H.; Zhang, S. Q. Hydrogenated Hematite Nanoplates for Enhanced Photocatalytic and Photo-Fenton Oxidation of Organic Compounds. *Inorg. Chem. Commun.* **2020**, *119*, 108040.

(47) Su, Z.; Liu, J. H.; Li, M.; Zhu, Y. X.; Qian, S. S.; Weng, M.; Zheng, J. X.; Zhong, Y. L.; Pan, F.; Zhang, S. Q. Defect Engineering in Titanium-Based Oxides for Electrochemical Energy Storage Devices. *Electrochem. Energy Rev.* **2020**, *3*, 286−343.

(48) Xu, H. M.; Hu, Y. W.; Huang, D.; Lin, Y.; Zhao, W. X.; Huang, Y. C.; Zhang, S. Q.; Tong, Y. X. Glucose-Induced Formation of Oxygen Vacancy and Bi-Metal Comodified Bi_5O_7Br Nanotubes for Efficient Performance Photocatalysis. *ACS Sustainable Chem. Eng.* **2019**, *7*, 5784−5791.

(49) Kresse, G.; Furthmüller, J. Self-Interaction Correction to Density Functional Approximation for Many Electron Systems. *Phys. Rev. B: Condens. Matter Mater. Phys.* **1996**, *54*, 11169.

(50) Kresse, G.; Joubert, D. From Ultrasoft Pseudopotentials to the Projector Augmented-Wave Method. *Phys. Rev. B: Condens. Matter Mater. Phys.* **1999**, *59*, 1758.

(51) Qiu, B.; Zhang, M.; Wu, L.; Wang, J.; Xia, Y.; Qian, D.; Liu, H.; Hy, S.; Chen, Y.; An, K.; Zhu, Y.; Liu, Z.; Meng, Y. S. Gas-Solid Interfacial Modification of Oxygen Activity in Layered Oxide Cathodes for Lithium-Ion Batteries. *Nat. Commun.* **2016**, *7*, 12108.

(52) Perdew, J. P.; Burke, K.; Ernzerhof, M. Generalized Gradient Approximation Made Simple. *Phys. Rev. Lett.* **1996**, *77*, 3865.

(53) Monkhorst, H. J.; Pack, J. D. Special Points for Brillouin-Zone Integrations. *Phys. Rev. B* **1976**, *13*, 5188.

(54) Henkelman, G.; Jónsson, H. Improved Tangent Estimate in the Nudged Elastic Band Method for Finding Minimum Energy Paths and Saddle Points. *J. Chem. Phys.* **2000**, *113*, 9978−9985.